Derived rotational and pressure-gradient seismic ocean-bottom data

Ohad Barak, Robert Brune, Paul Milligan and Shuki Ronen

ABSTRACT

In the Moere Vest acquisition a group of ocean-bottom nodes were deployed with a nominal spacing of two meters. We preprocessed the data of one shot line that traverses directly above these nodes. We then generated rotational and pressure-gradient data by differencing the geophone and hydrophone data of the adjacent nodes. We discuss the possibility of reverse-time propagation of such multicomponent seismic data.

INTRODUCTION

Rigid bodies in a three dimensional world have six degrees of freedom: three components of linear motion and three components of rotation. In the subsurface, the linear motions are the particle velocities and the rotations are the pitch, roll and yaw, as shown in the following table:

Axis	Displacement		Rotation	
Z	Vertical	v_z	Yaw	r_z
X	Radial	v_x	Roll	r_x
Y	Transverse	v_y	Pitch	r_y

where v_i are particle velocities along the axis, and r_i are rotation rates around the axis.

In ocean-bottom node acquisition, multicomponent geophones that are coupled to the seafloor record the vertical and the two horizontal components of particle velocity. Additionally, a hydrophone records the divergence of the wavefield $P = \kappa\,(\nabla \cdot \vec{u})$, where $\vec{u}$ are particle displacements and κ is the bulk modulus of the water to which the hydrophones are coupled. Rotations are a measurement of the curl of the wavefield $\vec{r} = \frac{1}{2}(\nabla \times \vec{v})$. However, as of yet there are no industry-grade solutions for recording rotational motion on the ocean bottom, though a few such recording stations have been deployed previously by Pillet et al. (2009).

The Moere Vest data includes a group of 26 ocean-bottom nodes, a "microspread," which have a unique geometry in that they are spaced at 2 m intervals. We estimated the three-component rotational motion by differencing adjacent geophones of these microspread nodes. Geophone differencing as a method of estimating the rotational motion signal has been shown previously in Barak et al. (2014a) and Edme et al. (2014). In the case of the microspread, the short 2 m interval between receivers ensures that most of the data is sampled well enough to prevent spatial aliasing, therefore, we assume that a differencing of the data recorded by adjacent nodes pertains to differences of displacements within half a wavelength.

Vassallo et al. (2012) use hydrophones together with pressure gradient sensors in marine streamer acquisition to interpolate the pressure wavefield in the crossline direction, between streamer cables. By differencing the hydrophone components of the adjacent nodes of the microspread, we similarly generated pressure gradient data. We can only obtain the two horizontal pressure gradients, since the nodes are all spread on the ocean-bottom, with no vertical separation.

Any differencing of data coming from physically separate sensors must be done with the caveat that we are in effect decreasing the signal to noise ratio in the resulting data. Each sensor may have a different coupling to the medium, reducing the reliability of the difference signal. Also, the data and the data difference are not collocated in space. Therefore, the data resulting from sensor differencing must be treated with a measure of suspicion. Barak et al. (2014b) discuss some of the problems associated with geophone differencing. Eventually, the only way to obtain a reliable recording of any physical quantity is to design a sensor that can measure that particular quantity at one point in space. The resulting rotational and pressure-gradient data can only be considered as an estimate of these data which would have been recorded with the adequate instrumentation. We would prefer not to use closely spaced receivers to measure rotations or pressure gradients in the field, but we do so here as a result of the special geometry of the microspread and the lack of the appropriate sensors.

Estimating rotational motion from geophone data

The stress-displacement relation for tangential stresses reads:

$$\sigma_{ij} = \mu \left(\partial_j u_i + \partial_i u_j \right), \tag{1}$$

where σ_{ij} are the tangential stresses, u_i are particle displacements and μ is the shear modulus.

At a free surface, or when going from a medium with shear strength to one without shear strength (such as the ocean-bottom interface), the tangential stresses σ_{ij} are zero. Therefore, assuming we have receivers laid out on a flat, horizontal sea bottom, we have

$$\begin{aligned} \partial_z u_y &= -\partial_y u_z, \\ \partial_z u_x &= -\partial_x u_z, \end{aligned} \tag{2}$$

meaning that the vertical derivative of the horizontal displacement component is equal to the horizontal derivative of the vertical displacement component.

Rotation is defined as the curl of the wavefield. Since our geophones record the time derivative of displacement (particle velocity), we use the time derivative of rotation, or rotation rate:

$$\vec{r} = \frac{1}{2}(\nabla \times \vec{v}) = \frac{1}{2}\Big(\hat{X}\left(\partial_y v_z - \partial_z v_y\right) + \hat{Y}\left(\partial_z v_x - \partial_x v_z\right) + \hat{Z}\left(\partial_x v_y - \partial_y v_x\right)\Big). \tag{3}$$

Substituting equation 2 into 3, we see that on the sea bottom

$$\begin{aligned} r_x &= \partial_y v_z, \\ r_y &= -\partial_x v_z, \\ r_z &= \frac{1}{2}\left(\partial_x v_y - \partial_y v_x\right), \end{aligned} \tag{4}$$

i.e., the horizontal rotation-rate components can be derived from the vertical geophones, and the vertical rotation-rate component can be derived from the horizontal geophones.

First-order in space elastic wave equation

The elastic wave equation for a homogeneous isotropic medium reads

$$(\lambda + \mu)\,\nabla\left(\nabla \cdot \vec{u}\right) + \mu\nabla^2\vec{u} = \rho\ddot{\vec{u}}, \tag{5}$$

where $\vec{u}$ are particle displacements, λ and μ are the Lamé parameters, and ρ is density. Using the vector identity $\nabla^2\vec{u} = \nabla\left(\nabla \cdot \vec{u}\right) - \nabla \times \left(\nabla \times \vec{u}\right)$, we get

$$(\lambda + 2\mu)\,\nabla\left(\nabla \cdot \vec{u}\right) - \mu\nabla \times \left(\nabla \times \vec{u}\right) = \rho\ddot{\vec{u}}. \tag{6}$$

Since pressure $P = \kappa\nabla \cdot \vec{u}$, we may now write the elastic wave equation using only first derivatives in space:

$$\frac{\alpha^2}{\kappa}\nabla P - \beta^2\nabla \times \vec{r} = \ddot{\vec{u}}, \tag{7}$$

where α and β are P and S wave velocities respectively, P is pressure and $\vec{r}$ are the rotations. Using the notation $\vec{p}$ for the pressure gradient vector ∇P, we have

$$\frac{\alpha^2}{\kappa}\vec{p} - \beta^2\nabla \times \vec{r} = \ddot{\vec{u}}. \tag{8}$$

We have effectively modified the elastic wave equation to a system with first order derivatives in space, with three different measurable vector physical variables: pressure gradients, rotations and acceleration of displacements.

MICROSPREAD GEOMETRY

There were two sets of fields in the SEGY files that indicated receiver positions. One of them was the "as-laid" positions, which are the coordinates of the underwater Remotely Operated Vehicle (ROV) that deployed the nodes on the sea bottom. The other set of receiver positions were calculated using the first-break arrival time at each node from all shots in the survey. Figure 1(a) shows these two sets of receiver positions.

Despite the fact that the first-break positions appear to have been manually manipulated, we opted to use these node positions for the microspread for two reasons:

1. The ROV positioning system becomes less accurate as the depth of deployment increases. In this case, the water depth was 1.6km.
2. We have video footage of the deployment taken by the ROV, which shows that the ROV operator placed the nodes on a regular grid, with little deviations.

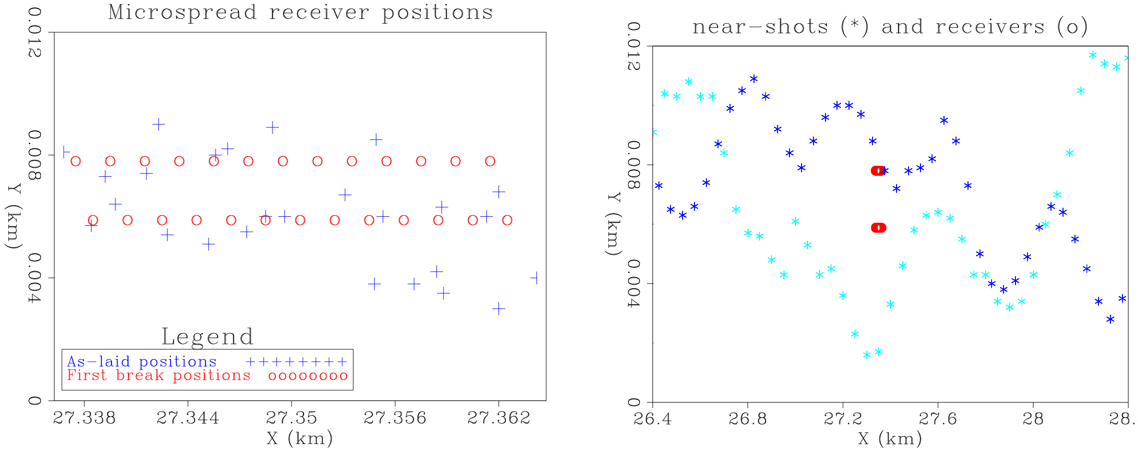

(a) (b)

Figure 1: (a) Microspread receiver "as-laid" positions vs. first-break positions. The length of the receiver line is 26 m, and the nominal receiver spacing is 2 m. (b) Microspread receiver positions (center of the figure, in red circles) with a subset of the shot positions from the two sail lines that are near the receivers. Note the exaggeration in the Y direction. The total shot line's length is 55 km. The largest crossline offset for these shot lines is 9 m, but over 90% of the shots have less than 5 m of crossline offset. Since the receivers are at a depth of 1.6 km, the acquisition is effectively 2D.

Figure 1(b) shows the microspread array in relation to the shot positions of the near-offset shots. As can be seen from this figure there were two shot lines, passing almost directly above the nodes. The shot interval of each shot line is 50m, and they are interlaced so that the effective shot spacing is 25m. However, in the following data figures in this paper, we used only one of the shot lines, since tidal variations between the times the shot lines were acquired cause static shifts to appear on receiver gathers. The total shot line length was 55km, with the microspread nodes positioned more or less in the center of the line. The water depth was nearly 1.6km, and the crossline offset was at most 9m, therefore the survey is effectively 2D.

INSTRUMENT DESIGNATURE

Figure 2(a) shows the instrument response functions for the geophones and the hydrophone. In Figure 2(b) the spectra of the responses are shown. Note that the hydrophone's response is flat from around 4Hz, while that of the geophone is flat from around 8Hz. Consequently, we would expect the geophone data to exhibit more of a phase shift before and after the designature process.

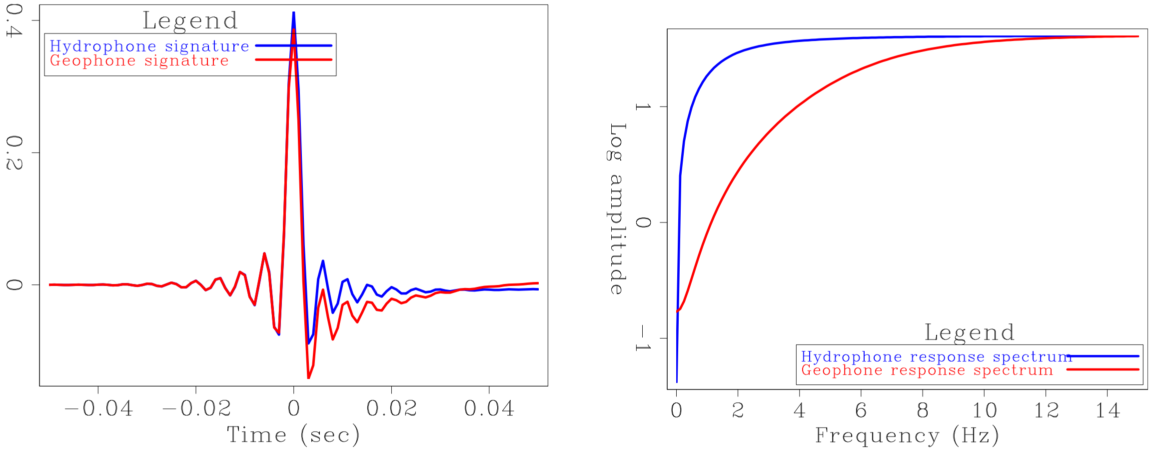

(a) (b)

Figure 2: Instrument signatures and their spectra. (a) Hydrophone (blue) and geophone (red) instrument response function vs. time. (b) Hydrophone (blue) and geophone (red) instrument amplitude response vs. frequency. Note how the hydrophone's frequency response is flat starting from around 4Hz, while the geophone response flattens around 8Hz. Both instrument responses remain flat until 204Hz, where a high-cut filter was applied. [**ER**]

Figure 3(a) shows a near-offset section of the hydrophone component of a receiver gather, after hyperbolic moveout was applied with water velocity. Blue wiggles indicate data before designature and red wiggles are after designature. Note how the designature caused the first break's energy to increase on the first negative lobe of the wavelet. There is also a slight phase shift concentrated on the first break. Figure 3(b) is vertical geophone gather before and after designature. The designature causes a much more marked change in this section. Much of the low frequency energy at $t = 1.1$s has been pushed up into the first break. Also, the low frequency bubble signal at $t = 1.19$s has shifted about 90°, and is now aligned with the bubble on the hydrophone section.

Figures 3(c) and 3(d) show the frequency spectrum of the stack of the moved out receiver gathers. The hydrophone's energy has been increased from about 4Hz and lower, while the vertical geophone's energy increased from 8Hz and lower. This is in accordance with the instrument frequency response in Figure 2(b).

A similar effect can be seen for the two horizontal geophones in Figures 4(c) and 4(d).

HORIZONTAL COMPONENT ALIGNMENT TO SURVEY COORDINATES

The horizontal components of the receivers of the microspread were not aligned with the survey's shot geometry. As each node is placed on the seafloor by the ROV, their alignment is not identical. For further processing, we required that the coordinates of the horizontal data components match those of the survey, and that they be consistent for all nodes. Consequently, a rotation of the horizontal components around the vertical axis was required. To gauge the amount of rotation, we first applied hyperbolic moveout to the data, then took a window of 100 milliseconds around the first break. We rotated the horizontal components of each node, and then stacked the result and saw at what degree of rotation did we get a minimal amount of energy on the v_y component. The logic is that since the shot line has very little crossline offset with the microspread array, the first break should contain minimal energy in the crossline direction.

Figures 5(a) and 5(b) show the average amplitude of the first break on the two horizontal components of each node, as a function of rotation angle. We see that all the nodes appear to require a rotation of approximately 20° to align them with the survey.

Figure 6(a) is the v_y component before the rotation to survey coordinates, and Figure 6(b) is the same gather after rotation. Note how the first break's energy has been significantly weakened, along with much of the energy of the bubble.

GENERATION OF 9C DATA

To generate the three-component rotation-rate data, we used a finite-difference approximation to equations 4:

$$\begin{aligned}
r_y &\approx \frac{1}{\Delta x}\left(v_z^{i\Delta x, j\Delta y} - v_z^{(i+1)\Delta x, j\Delta y}\right), \\
r_x &\approx \frac{1}{\Delta y}\left(v_z^{i\Delta x, (j+1)\Delta y} - v_z^{i\Delta x, j\Delta y}\right), \\
r_z &\approx \frac{1}{4}\left[\frac{1}{\Delta x}\left(v_y^{i\Delta x, j\Delta y} - v_y^{(i+1)\Delta x, j\Delta y}\right) + \frac{1}{\Delta x}\left(v_y^{i\Delta x, (j+1)\Delta y} - v_y^{(i+1)\Delta x, (j+1)\Delta y}\right)\right] \\
&+ \frac{1}{4}\left[\frac{1}{\Delta y}\left(v_x^{i\Delta x, (j+1)\Delta y} - v_x^{i\Delta x, j\Delta y}\right) + \frac{1}{\Delta y}\left(v_x^{(i+1)\Delta x, (j+1)\Delta y} - v_x^{(i+1)\Delta x, j\Delta y}\right)\right]. \quad (9)
\end{aligned}$$

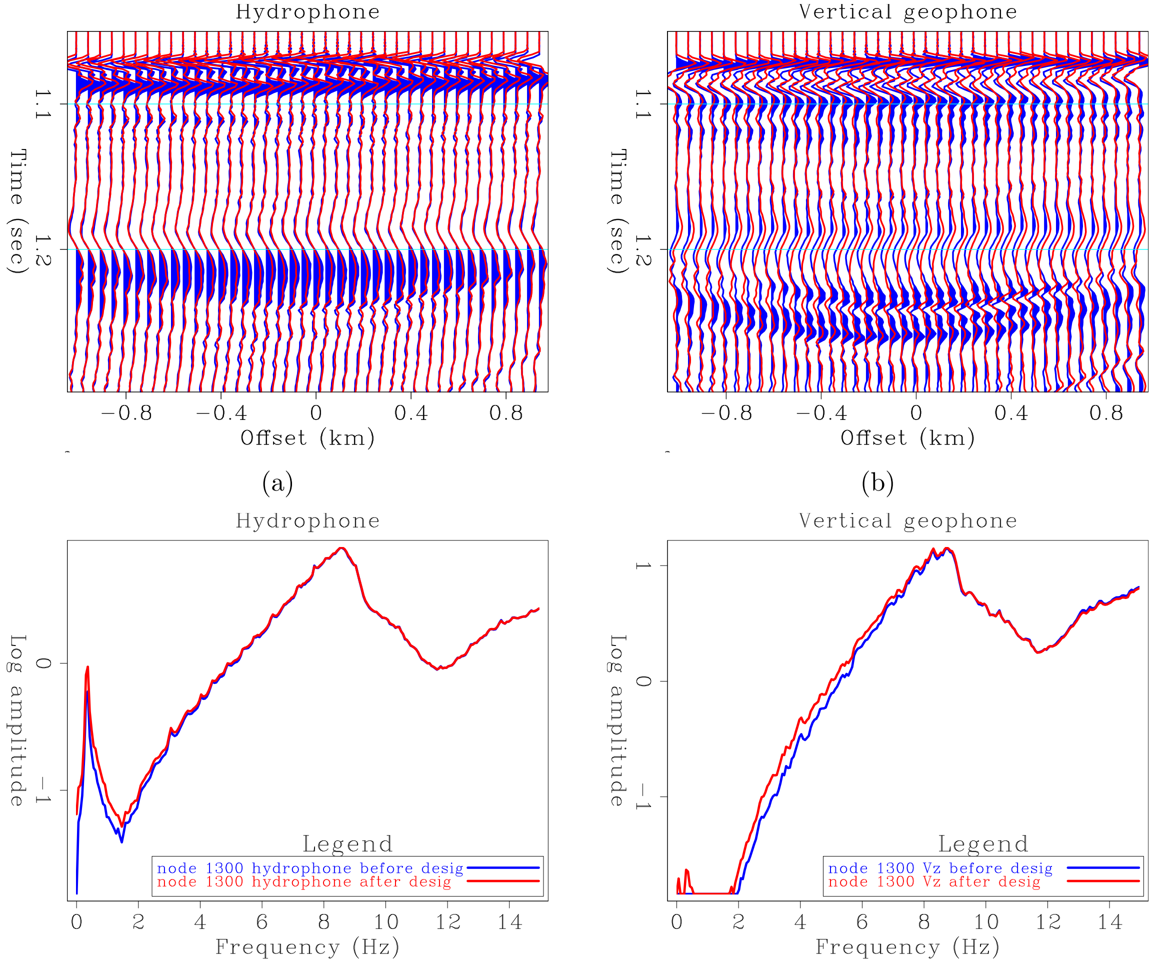

(a) (b)

(c) (d)

Figure 3: Data components of a receiver gather after hyperbolic moveout with water velocity, before and after instrument designature. (a) Hydrophone before (blue) and after (red) designature. (b) Vertical geophone before (blue) and after (red) designature. (c) and (d) are the log of the amplitude spectrum of the hydrophone and vertical geophone, respectively. Observe the increase in the lower amplitudes, particularly for the 8Hz geophone. The spike at 0.4Hz on the hydrophone is sea-swell ambient noise. Observe also how after designature, the low frequency bubble at $t = 1.19$s on the vertical geophone has an opposite polarity to the bubble on the hydrophone. Similarly, the direct arrival at $t = 1.08$s has an opposite polarity on the hydrophone vs. the vertical geophone. [**CR**]

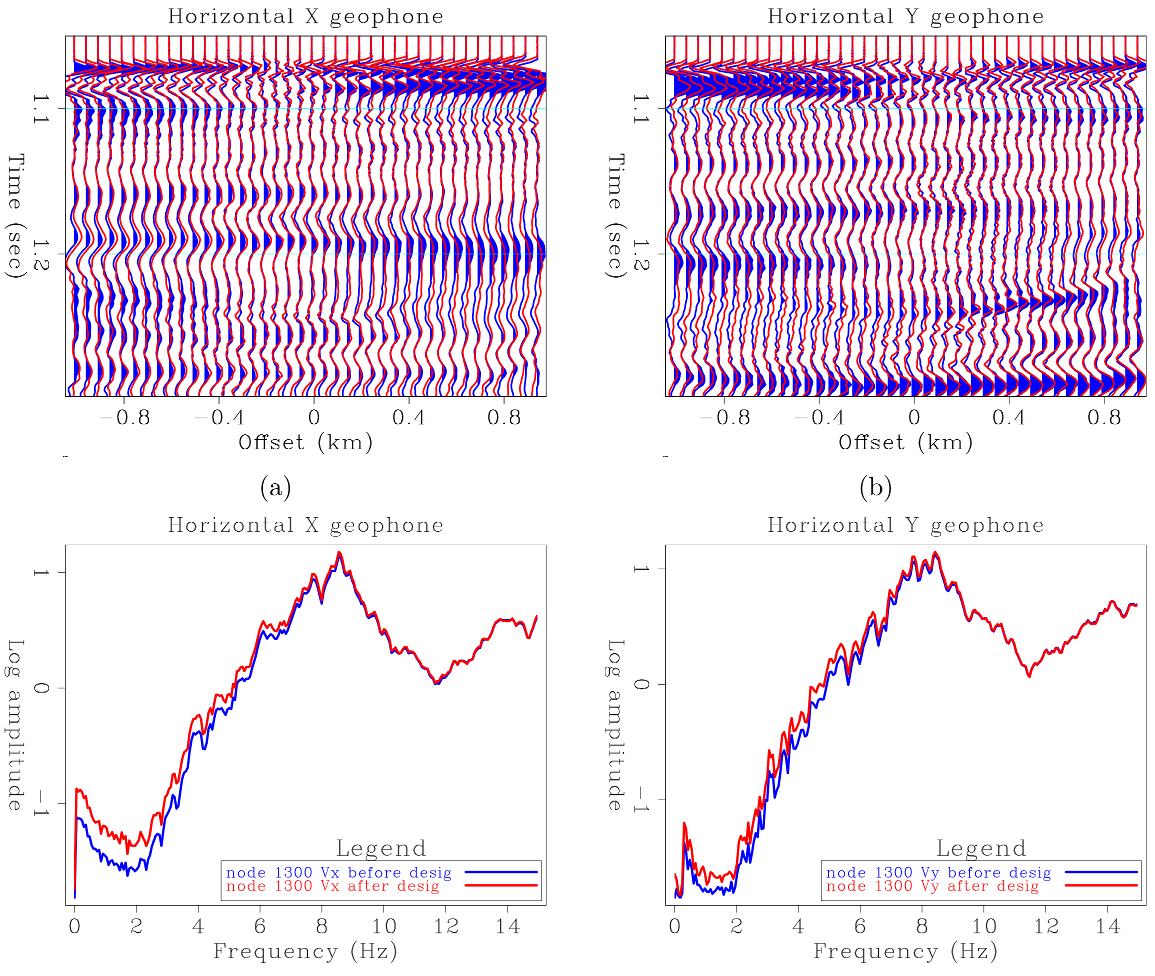

(a) (b)

(c) (d)

Figure 4: Data components of a receiver gather after hyperbolic moveout with water velocity, before and after instrument designature. (a) Horizontal inline geophone before (blue) and after (red) designature. (b) Horizontal crossline geophone before (blue) and after (red) designature. (c) and (d) are the log of the amplitude spectrum of these two component. Note that the horizontal geophones in this figure are not yet rotated to the true radial and transverse directions, however the geophone inline ('X') component is only about 20° away from the radial direction. [**CR**]

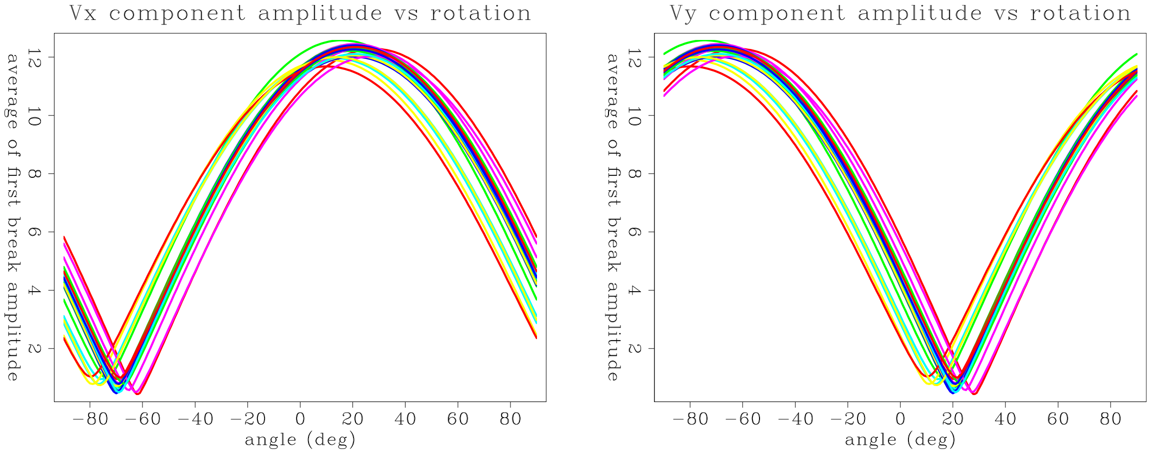

(a) (b)

Figure 5: Average amplitude of a 100 millisecond window around the first break, as a function of the rotation of the horizontal components around the vertical axis. (a) v_x component. (b) v_y component. Each line in the graph is one of the 26 nodes of the microspread. It appears that in order to minimize the energy on the v_y component and thus have v_y perpendicular to the 2D shot line and v_x parallel to it, the nodes need to be rotated by about 20^o. [**CR**]

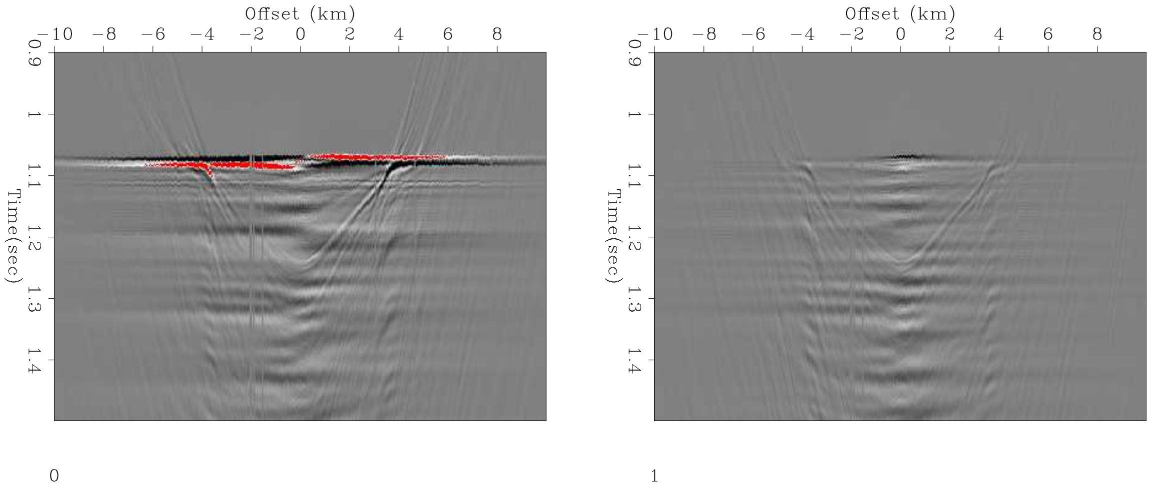

(a) (b)

Figure 6: The v_y component of the receiver gather at node 1300 after hyperbolic moveout with water velocity, (a) before alignment to crossline direction, and (b) after alignment to crossline direction. Since the survey geometry for these data was effectively 2D, the rotation should minimize the first break's ($t = 1.08$s) energy on the v_y component. [**CR**]

Δx is the inline spacing between neighbouring nodes, and Δy is the crossline spacing. The order of subtraction operations in the differencing equations 9 were done so that the direction of the rotational axes would be the same as the linear geophone components, according to right-hand rule.

Figures 7(a),7(c) and 7(e) are the vertical (v_z), inline (v_x) and crossline (v_y) geophone components of the receiver gather of node 1730. Figures 7(b),7(d) and 7(f) are the yaw (r_z), roll (r_x) and pitch (r_y) rotational components. Notice that adjacent to each one of the geophone components is the rotational component around that geophone's axis.

We are not displaying the direct arrival and some of the associated bubbles that are between $t = 1.08$s and $t = 1.75$s. The water-bottom multiple appears at $t = 3.25$s, and can be seen well on the v_z and v_x sections.

The v_z component seems to contain mostly high-frequency reflections with a moveout consistent with P-wave velocity, but there are some lower frequency events apearing after every P reflection that have a much slower moveout. These events are commonly called "VZ noise", and may be caused by shear-wave scattering off the node body itself as a result of the incident P-wave. The v_x component contains mostly those shear-wave events, but some of the P-wave reflections apparent on v_z are also visible. The v_y component is much weaker than the other two geophone components, but a shear-wave event similar to the one on the v_x component at $t = 3.3$s is visible.

Observing the rotational components, we see that the one with the greatest energy is r_y. This fits with our expectation. Since the survey geometry is practically 2D, most of the linear motion should occur in the vertical and inline directions, which means that most of the rotational motion should occur around the crossline direction. Note also the generally increased noise level on the rotational components.

Compare the v_z and r_y components, and observe how the P-waves are almost not visible on r_y, even though this section was obtained using two vertical geophones. This indicates that the P-waves generate a similar response on adjacent vertical geophones, and are removed by the differencing. Another way of saying the same thing is that the P-waves do not generate a rotational deformation of the surface. Instead, we see a section that is more similar to v_x, with events that have shear-wave moveouts (though slightly delayed compared to v_x). Shear waves, as their name suggests, generate a shear deformation of the surface, which expresses itself as rotational motion. Therefore, rotational data should preferentially record shear waves, and indeed the P events on the r_y component are much weaker than those visible on the v_z and v_x components.

The r_x rotational component seems to also contain some shear wave events related to the P-waves that hit the node. They are weaker than the events on r_y, indicating that if these are indeed the result of scattered shear waves, then these waves are causing mainly rotation around the crossline axis. The r_z section is the weakest of the rotations. This component should record events that cause a horizontal deformation around the vertical axis, i.e. Love or SH waves, neither of which seem particularly likely in this environment. What energy is on the r_z component seems to also be related to the incident P-waves.

We note that the nodes were not corrected for tilt. Each node is tilted approximately 2 to 4 degrees away from the vertical according to tiltmeters on the node bodies. Therefore, there may be leakage of the vertical motion into the horizontal geophones, and consequently into the r_z component.

To generate pressure-gradient data, we differenced the hydrophone component of the nodes:

$$\begin{aligned} p_x &\approx \frac{1}{\Delta x}\left(P^{(i+1)\Delta x,j\Delta y} - P^{i\Delta x,j\Delta y}\right), \\ p_y &\approx \frac{1}{\Delta y}\left(P^{i\Delta x,(j+1)\Delta y} - P^{i\Delta x,j\Delta y}\right). \end{aligned} \tag{10}$$

Figure 8(a) and 8(b) are the inline (p_x) and crossline (p_y) pressure gradients. Figure 8(c) is the hydrophone component. Note how the pressure gradients are much noisier than the hydrophone. This may be due to the P-waves having very low wavenumbers, so that there is not much of a difference between the hydrophone signal on adjacent nodes, and therefore differencing them increases the noise at the expense of the signal. This is especially true for the P_y component. If we consider the propagation path of the P-waves and the 2D survey geometry, we see that indeed there should not be a great difference in the pressure recorded by two nodes that are separated by 2 m in the crossline direction.

It is interesting that on the pressure-gradient sections we can see events with shear-wave moveouts at $t = 2.7$s that are not apparent on the hydrophone. This indicates that the shear events (whether they be caused by an actual shear reflection or a shear-wave scattering off the node body), are generating a pressure gradient without appearing on the pressure sensor as prominently as P-waves. This, in turn, indicates that some shear-wave energy is being recorded by the hydrophone.

DISCUSSION

In current seismic acquisition, geophones record only the displacements but not rotations, while hydrophones record the pressure but not its gradient. However, with the advent of a new generation of seismic sensors, these physical values will be measurable at each receiver position, giving us ten-component seismic data (1 pressure, 3 displacements, 3 rotations and 3 pressure gradients). Prototype pressure-gradient sensors are being developed, and rotation sensors exist and have seen some very limited use in seismic test surveys. Water accelerometers that effectively measure the pressure gradient in water have already been used widely in the exploration industry.

Consider an algorithm that propagates an elastic wavefield comprising the measured physical variables of displacements, pressure, pressure gradient and rotations

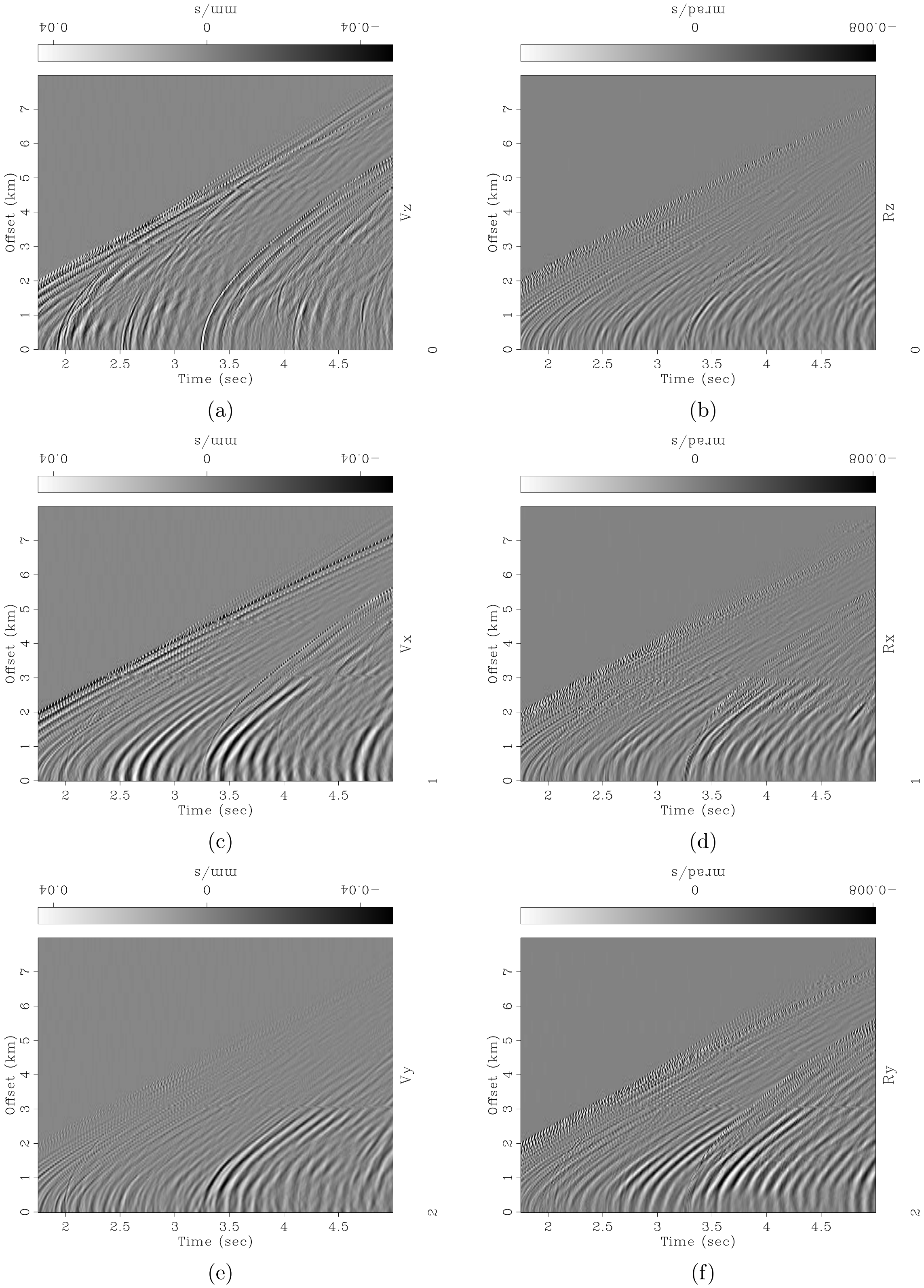

(a) (b)

(c) (d)

(e) (f)

Figure 7: Six-component receiver gather of node 1730. (a) Vertical particle velocity v_z. (b) Yaw rotation r_z. (c) Inline particle velocity v_x. (d) Roll rotation r_x. (e) Crossline particle velocity v_y. (f) Pitch rotation r_y. [**CR**]

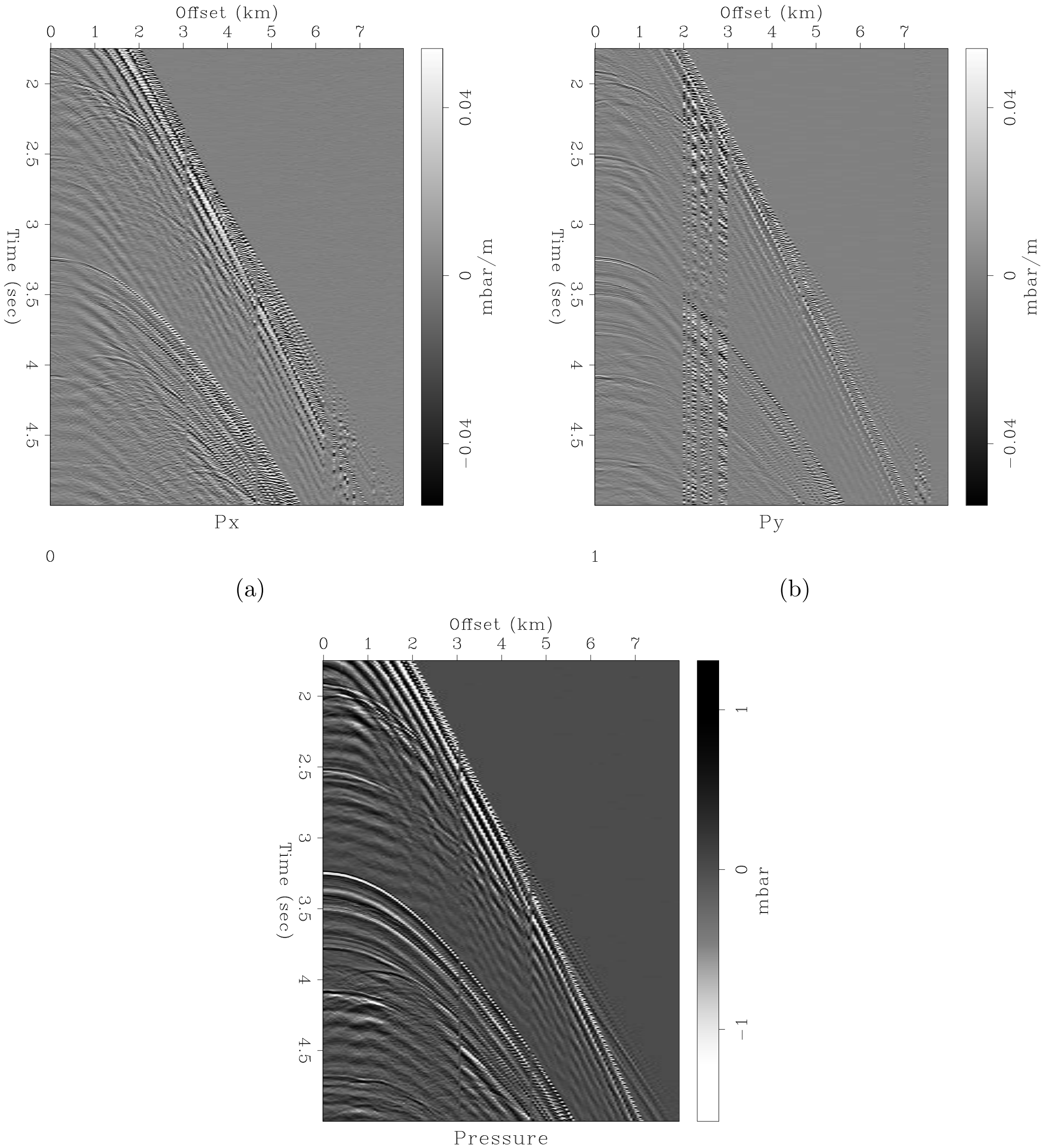

(a) (b)

(c)

Figure 8: Pressure and pressure gradient for receiver gather of node 1730. (a) Pressure gradient in the inline direction P_x. (b) Pressure gradient in the crossline direction P_y. (c) Pressure. [**CR**]

(equation 8). Since both displacements and their spatial derivatives are recorded (pressure, pressure gradient and rotations), injecting them into an elastic wavefield propagator will generate waves that propagate not only in reverse time, but also in the opposite direction to their arrival at the receivers. This characteristic is used for deghosting acoustic marine streamer data by Vassallo et al. (2012). In the case of ocean-bottom seismic, this has the added advantage of separating the upgoing from the downgoing wavefield during elastic reverse-time propagation of the receiver data. This dismisses the need to separate the ocean-bottom data into upgoing and downgoing wavefields, using such methods as PZ summation (Barr and Sanders, 1989), which are commonly applied before imaging with ocean-bottom data (Wong et al., 2011).

Furthermore, injection of the displacement data and its derivatives will prevent mode conversion at the injection point, where P waves in the data are converted to S waves (and vice versa) immediately upon injection into the modeled wavefield. Such spurious modes can generate additional artifacts in the resulting image.

SUMMARY

We preprocessed seismic ocean-bottom node data so as to remove the receiver instrument signature and align the horizontal geophone components to the 2D survey coordinates. We used the fact that the receivers were deployed with small spacings to difference their data and estimate the rotational-motion and pressure-gradient data that would have been recorded had we instruments that were able to measure these physical variables directly on the ocean-bottom, thereby generating nine-component data. We anticipate that ten-component data comprising displacements, pressure, pressure gradient and rotations will improve seismic imaging with ocean-bottom data.

ACKNOWLEDGEMENTS

We thank Seabed Geosolutions for releasing the field data.

REFERENCES

Barak, O., S. de Ridder, J. Giles, P. Jaiswal, S. Ronen, and R. Brune, 2014a, Six-component seismic land data acquired with geophones and rotation sensors: Wave-mode separation using 6C SVD: SEG Technical Program Expanded Abstracts 2014, 1863–1867.

Barak, O., P. Jaiswal, S. de Ridder, J. Giles, R. Brune, and S. Ronen, 2014b, Six-component seismic land data acquired with geophones and rotation sensors: Wave-mode separation using 6C SVD : SEP-Report, **152**, 335–350.

Barr, F. and J. Sanders, 1989, Attenuation of water column multiples using pressure and velocity detectors in a water bottom cable: SEG Technical Program Expanded Abstracts 1989, 653–656.

Edme, P., E. Muyzert, and E. Kragh, 2014, Efficient land seismic acquisition sampling using rotational data: 76th EAGE Conference and Exhibition, Seismic Noise Attenuation Session.

Pillet, R., A. Deschamps, D. Legrand, J. Virieux, N. Bethoux, and B. Yates, 2009, Interpretation of broadband ocean-bottom seismometer horizontal data seismic background noise: Bulletin of the Seismological Society of America, **99**, 1333–1342.

Vassallo, M., K. Eggenberger, D. J. van Manen, K. Ozdemir, J. Robertsson, and A. Ozbek, 2012, Contributions of the horizontal and vertical components of particle velocity in 3D pressure wavefield reconstruction on dense receiver grids using generalized matching pursuit: SEG Technical Program Expanded Abstracts, 1–5.

Wong, M., S. Ronen, and B. Biondi, 2011, Leastsquares reverse time migration/inversion for ocean bottom data: A case study: SEG Technical Program Expanded Abstracts 2011, 2369–2373.